POLITECNICO DI TORINO
Repository ISTITUZIONALE

Computational Synthesis of Histological Stains: A Step Toward Virtual Enhanced Digital Pathology

Terms of use:

Publisher copyright

(Article begins on next page)

14 October 2024

RESEARCH ARTICLE OPEN ACCESS

Computational Synthesis of Histological Stains: A Step Toward Virtual Enhanced Digital Pathology

Massimo Salvi[1] | Nicola Michielli[1] | Lorenzo Salamone[1] | Alessandro Mogetta[1] | Alessandro Gambella[2] |
Luca Molinaro[3] | Mauro Papotti[4] | Filippo Molinari[1]

[1]Biolab, PoliToBIOMed Lab, Department of Electronics and Telecommunications, Politecnico di Torino, Turin, Italy | [2]Pathology Unit, Department of Medical Sciences, University of Turin, Turin, Italy | [3]Division of Pathology, A.O.U. Città Della Salute e Della Scienza Hospital, Turin, Italy | [4]Division of Pathology, Department of Oncology, University of Turin, Turin, Italy

Correspondence: Massimo Salvi (massimo.salvi@polito.it)

ABSTRACT

Histological staining plays a crucial role in anatomic pathology for the analysis of biological tissues and the formulation of diagnostic reports. Traditional methods like hematoxylin and eosin (H&E) primarily offer morphological information but lack insight into functional details, such as the expression of biomarkers indicative of cellular activity. To overcome this limitation, we propose a computational approach to synthesize virtual immunohistochemical (IHC) stains from H&E input, transferring imaging features across staining domains. Our approach comprises two stages: (i) a multi-stage registration framework ensuring precise alignment of cellular and subcellular structures between the source H&E and target IHC stains, and (ii) a deep learning-based generative model which incorporates functional attributes from the target IHC stain by learning cell-to-cell mappings from paired training data. We evaluated our approach of virtual restaining H&E slides to simulate IHC staining for phospho-histone H3, on inguinal lymph node and bladder tissues. Blind pathologist assessments and quantitative metrics validated the diagnostic quality of the synthetic slides. Notably, mitotic counts derived from synthetic images exhibited a strong correlation with physical staining. Moreover, global and stain-specific metrics confirmed the high quality of the synthetic IHC images generated by our approach. This methodology represents an important advance in automated functional restaining, achieved through robust registration and a model trained on precisely paired H&E and IHC data to transfer functions cell-by-cell. Our approach forms the basis for multiparameter histology analysis and comprehensive cohort staining using only digitized H&E slides.

1 | Introduction

Histological staining is a fundamental technique in pathology used for the analysis of biological tissues and the diagnosis of pathologies. Pathologists utilize various staining modalities to examine specimens from both morphological and biochemical/functional perspectives. These stains highlight different tissue characteristics, allowing to extract valuable information for disease grading, classification, and diagnosis. The most common and widespread stain for histopathological assessment is hematoxylin and eosin (H&E), which facilitates the comparison of morphological and cellular features across different tissues and pathological conditions. In addition to H&E, special histochemical stains like periodic acid-Schiff (PAS), trichrome, or immunohistochemical (IHC) stainings are employed to further investigate the tissue properties [1, 2].

Obtaining multiple serial tissue sections for H&E and subsequent special stains allows fast parallel processing but is limited by lack of precise correspondence and risk of exhausting diagnostic material. A potential alternative to this approach is represented by cutting a single section which is initially stained for

H&E and subsequently destained and restained for histochemical or IHC stains based on specific requests. This comprehensive approach allows to spare tissue, simultaneously observe the same cellular structures with different stains, and obtain both morphological and functional features. Indeed, it enables the assessment of cell and tissue morphology from H&E staining and the identification of specific proteins or cellular structures from the special or IHC stain, thereby highlighting aspects such as cell proliferation and mitotic activity [3]. However, this process faces practical challenges. The multi-step staining protocol, which requires removing the initial stain, is time-consuming and often not compatible with the daily workload of a pathology unit. Furthermore, the destaining process required aggressive chemical phases which may impact tissue preservation and stain reliability [4].

A clinical use case where both H&E and IHC stains are required for diagnostic and prognostic purposes is the detection and quantification of mitoses. Mitosis assessment is a common and essential procedure in pathology, especially in the neoplastic setting where the mitotic count (i.e., the presence and density of cells undergoing cell division) is an essential parameter to define tumor aggressiveness, prognosis, and treatment strategy [5]. The commercially available immunohistochemical marker phospho-histone H3 (PHH3) has emerged as a valuable assay for mitotic detection [6, 7]. This IHC marker specifically highlights the phosphorylated form of histone H3, which is a critical protein involved in chromosomal condensation during mitosis, thus targeting all cells in the process of mitosis and ultimately allowing a specific mitotic count. The integration of morphological information from H&E staining with the specific mitotic activity highlighted by PHH3 staining provides a more comprehensive understanding of tumor characteristics, aiding in accurate diagnosis and personalized patient management [8].

The optimal diagnosis is achieved when the same slide is analyzed using H&E and IHC stainings, allowing for an assessment of the same cellular structures from both morphological and functional perspectives. However, this approach is expensive and resource-intensive for laboratory technicians and pathologists. Figure 1a shows a sample image pair of the same slide first stained with H&E and then restained using PHH3, while Figure 1b shows adjacent tissue sections.

The introduction of digital pathology has revolutionized the way tissue slides are handled, allowing for digitization, storage, and easy sharing of images between different centers [9]. In this context, artificial intelligence (AI) techniques can extract hidden quantitative information from digital histopathology images [10]. The integration of AI-based methods aims to reduce pathologist workload and improve diagnosis formulation [11]. Deep learning is now enabling digital replacement of parts of the histological staining procedure for a more sustainable, rapid and cost-effective pipeline in histopathology. In virtual staining, histological stains are created by training deep networks to digitally convert unstained or unlabeled tissue sections into stained/labeled images or through the transformation of images of an already stained tissue sample into another type of stain [12]. One emerging area of research in this field involves generative adversarial networks (GANs), which have shown promise in automatically performing virtual restaining. Starting from real images stained with a specific dye, these GANs can generate synthetic images that simulate different stainings. This novel approach holds great potential for transforming clinical analysis of histopathological images [13].

Despite its great potential, the virtual restaining process faces several key challenges. First, paired generative models require paired image data with corresponding cells in the two histological stains. However, obtaining such precisely matched paired data is difficult, as previously explained. Conversely, unpaired models do not require exactly matching source and target domain images, enabling style transfer but without functional content transfer capabilities [14]. In the case of consecutive slides, misalignments arise due to variations in slide preparation techniques and differences in the scanned field of view. Addressing this problem requires an initial registration phase to align the image datasets [15–17]. Validating that the restaining process successfully transfers the correct functional information, and not just a visual style, is also mandatory. However, quantitative evaluation in this area remains limited. While some studies rely on pathologists' evaluations, few works compute full-reference quantitative metrics or algorithm-based feature analysis [13].

The purpose of this work is to develop and evaluate a novel experimental automated framework for functionally restaining
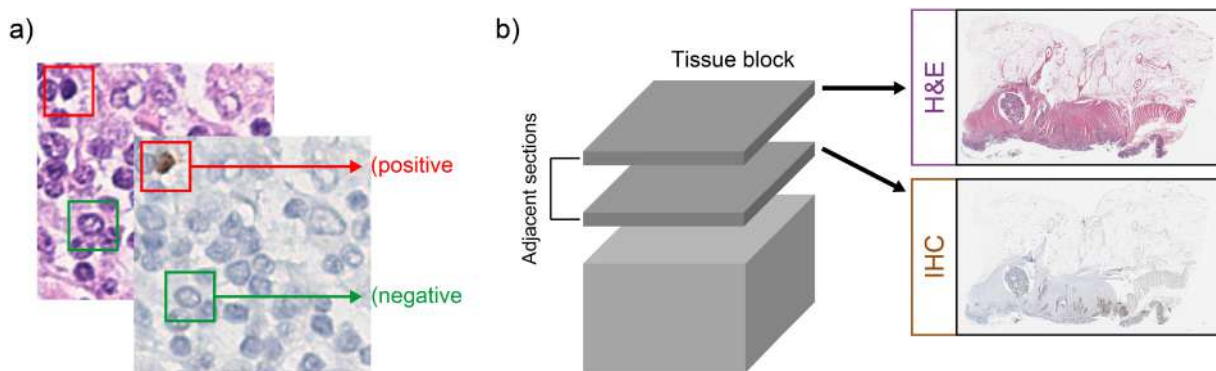

FIGURE 1 | (a) H&E-IHC image pair acquired by chemically destaining and restaining the same tissue section. (b) Matched H&E and IHC-stained slides derived from two consecutive tissue sections.

digitalized microscopic tissue slides. The proposed model is based on a multi-stage registration framework that aligns histological slices and a generative model, trained on paired data, that creates realistic PHH3 synthetic images, enabling the transfer of functional information at the cell level. To the best of our knowledge, this is the first study which validates each step of the pipeline, both the multi-stage registration process and the final virtually restained image quality. The main contributions of this work are summarized as follows:

- A multi-stage registration approach is employed to achieve precise pixel-wise matching between cellular and subcellular structures from H&E and IHC slides. Accurate image alignment is critical, as it ensures corresponding structures are properly mapped during virtual restaining.

- A deep leaning-based generative model is trained on paired data, enabling the transfer of functional information. Unlike prior methods focused solely on stain style-transfer, our model considers both morphological and functional attributes, learning cell-to-cell mappings from training data.

- Quantitative evaluation of both registration and restaining stages is conducted. Global image quality assessment (IQA) metrics, landmark-based target registration error (TRE) and novel IHC-based local metrics provide a thorough assessment of the registration accuracy and quality of the restaining results.

- Synthetic images are evaluated by an expert pathologist for mitotic count and compared to counts from real IHC images. This clinical validation provides valuable insight into the accuracy and reliability of virtual restaining for diagnostic applications.

2 | Literature Review

Deep learning-based virtual staining and restaining methods can be categorized into two main groups based on their image transformation approach:

1. *Label-free virtual staining*: this process involves digitally converting unstained or unlabeled tissue sections into stained/labeled images. Rivenson et al. [18] performed virtual H&E, trichrome and silver staining on autofluorescence images, with qualitative validation by pathologists but no quantitative metrics. Li et al. [19] transferred unlabeled tissue into H&E, picrosirius and orcein stained versions, qualitatively validated on rat sections after rigid registration. Pillar and Ozcan [20] used a GAN for virtual H&E, trichrome, silver and HER2 staining, assessed by pathologists without quantification. Zhang et al. [21] presented a virtual staining framework able to stain in H&E defocused autofluorescence images of unlabeled tissue. Standard intensity-based quantitative metrics were computed during validation. Bai et al. [22] transformed unlabeled breast tissue into HER2 stained images. Synthetic images were assessed by three expert pathologists in terms of HER2 score and staining quality. Salido et al. [23] compared models for virtual H&E staining of breast tissue, with quantitative and manual registration analysis. Rana et al. [24] proposed a deep learning

model to generate H&E-stained prostate cancer images form unstained counterparts. The virtual staining method was quantitatively and clinically validated, but no analysis was carried out for the registration process. Li et al. [25] transformed autofluorescence images of label-free autopsy tissue sections into H&E-stained versions, using a standard U-Net architecture to predict the displacement vector field. Pillar et al. [26] published a comprehensive review of the latest advancements in generating pseudo-stained outputs from non-fixed human tissue; the review is limited to standard H&E stain.

2. *Stain-to-stain transformations or virtual restaining*: methods which computationally transform the image of an already stained tissue (e.g., stained with H&E) into another stain (special histochemical or IHC stains) without physically tampering with the slides. Xu et al. [14] proposed a conditional CycleGAN to transform H&E-stained images into IHC synthetic images. The network was trained with unpaired data and the results were not quantitatively assessed. Similarly, Liu et al. [27] proposed an unpaired stain transfer method using pathology-consistent constrained GANs for transferring between H&E and Ki-67-stained images. They utilize cycle consistency and pathology-specific losses to enable unpaired training and introduce pathological representation networks to enforce consistent pathological features. Mercan et al. [28] proposed a virtual staining framework to generate synthetic phospho-histone H3 images from H&E-stained breast images. No quantitative metrics were assessed; the validation was only performed by training a mitosis classifier on GAN feature maps. De Haan et al. [4] proposed a stain-to-stain transformation framework to create three additional special stains (PAS, Masson's trichrome and Jones silver stain) from existing H&E tissue sections. Results are limited to nonneoplastic kidney tissue and were evaluated by three nephropathologists in terms of kidney disease diagnoses and quality scores. Both image co-registration step and virtual restaining were not quantitatively assessed. Liu et al. [29] proposed a breast cancer immunohistochemical (BCI) dataset and a pyramid pix2pix image-to-image translation model to synthesize HER2 breast sections from paired H&E-stained images. A semi-automatic registration method is employed to align image pairs. Standard quantitative evaluation metrics were computed for the quality of generated images. Vasiljević et al. [30] analyzed the virtual stain-to-stain translation of four stains (Jones H&E, Sirius red, and IHC stains like CD68 and CD34) to demonstrate that relatively small changes in CycleGAN-based methods could have a great impact on translation quality. Yan et al. [31] proposed a study based on unpaired data for Masson's trichrome stained image generation from the corresponding H&E-stained images. Zhang et al. [32] proposed a staining transfer framework to generate virtual functional staining from H&E to several combinations of IHC stains, including ER/PR/HER2 in breast tissue and Ki67/CC10/proSPC in mouse lung. Gadermayr et al. [33] proposed a GAN-based stain-translation of PAS to acid fuchsin orange G (AFOG) stain and IHC stains like Col3 and CD31 on kidney tissue images, to facilitate segmentation applications in digital pathology.

3 | Materials and Methods

In this paper, we present our method to generate synthetic PHH3 images from H&E-stained ones. Figure 2 summarizes the overall flowchart of the proposed approach. Our method is based on a multi-stage registration framework that aligns histological H&E-IHC tissue pairs and a GAN-based model is trained on registered data to create realistic PHH3 synthetic images.

3.1 | Dataset

Tissue sections from inguinal lymph nodes and bladder were cut, stained with H&E and scanned with a Hamamatsu NanoZoomer S210 Digital slide scanner at 40× magnification (0.221 μm/pixel). Subsequently, the H&E-stained slides were destained and restained with PHH3, then rescanned at same magnification. This process resulted in dual-stained H&E-PHH3 slides representing the same tissue section. Bladder tissue samples were used as an independent blind test set for validation purposes.

3.2 | Multi-Stage Registration Framework

Registration is necessary to spatially align H&E-PHH3 image pairs. We employed the VALIS (Virtual Alignment of pathoLogy Image Series) method developed by Gatenbee et al. [34, 35]. VALIS first performs a macro-registration through a cascade of rigid and affine transformations on lower magnification. Then, it conducts micro-registration at higher magnifications by computing a localized pixel-wise displacement field. For successful registration, the authors recommend converting RGB images to the CAM16-UCS color space format prior to alignment to standardize hue and colorfulness [36]. VALIS macro-registration estimates global matrix transformations while micro-registration refines alignment at higher resolution. However, micro-registration requires the images to be partially aligned beforehand. For a 34×42k pixels image pair at 20× magnification, VALIS registration takes approximately 45 min; at 10× or higher, attempting micro-registration of the full-size images exceeds the memory capacity of a 64 GB workstation. Therefore, applying VALIS full resolution registration was deemed unfeasible for our dual-stained slides. In this work, we employed a multi-stage registration framework based on VALIS method, to achieve pixel-level matching using a two-step process:

- 1st stage: tissue sections were initially registered with VALIS using a 1.25× working magnification for macro-registration and 2.5× for micro-registration. CAM16-UCS conversion was skipped as no performance decrease was observed, saving 23% of RAM and computational time.

- 2nd stage: after the 1st registration stage, a luminance correction approach proposed in our previous study [37], was employed to optimize and balance the illuminant condition of unstained regions. Then, several image fields with at least 80% of tissue area were extracted from preregistered slides. The VALIS method was finally applied to full resolution (40×) non-pyramidal image fields to achieve cellular structure matching.

This computationally efficient two-step framework enables the proposed virtual restaining task. All registration steps with varying magnifications from the original tissue sections until the non-pyramidal image fields are quantitatively evaluated in the following sections.

3.3 | Data Preparation

In PHH3 staining, 3,3′-diaminobenzidine (DAB) provides brown-colored staining of cells in mitotic activity and hematoxylin is employed as a counterstain in blue color [6]. As mitotic cells are far fewer than normal cells, a traditional patch extraction risks producing a highly unbalanced training set with predominately negative hematoxylin-stained patches. For this reason, we implemented a DAB-driven patch extraction process that focuses on accurately capturing examples of the mitosis cells stained brown by DAB. Our targeted extraction approach involves the following steps:

1. Cells in mitosis are segmented from red-blue channels using global thresholding and their centroid is computed.

2. A 256×256 window scrolls each IHC tile: each time the centroid of a DAB cell falls within the window, multiple
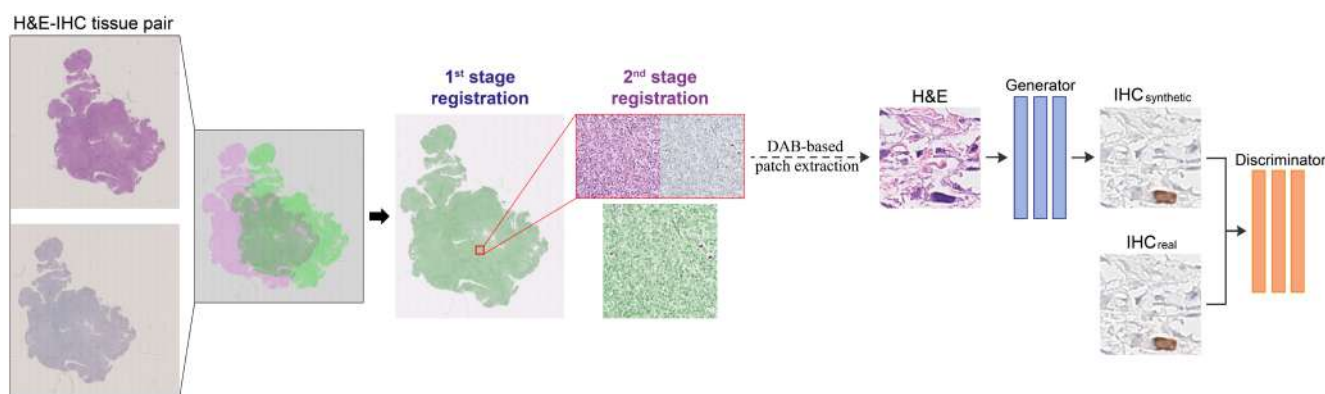

FIGURE 2 | Workflow of the proposed method. A multi-stage registration approach is employed to align whole tissue sections (1st stage) and to achieve precise pixel-wise matching between cellular structures (2nd stage). Registered paired image data are used to train a GAN-based virtual restaining model enabling the transfer of functional information.

patches are extracted by moving the region of interest (ROI) in all directions. In this way, the same DAB-stained cell is placed in different locations of the patch, as shown in Figure 3a.

3. To enhance diversity, 20 patches are randomly selected from those obtained per centroid, maximizing distance between list positions.

4. Corresponding H&E patches are extracted using the same coordinates, as reported in Figure 3b.

Additionally, nonoverlapping 256×256 patches lacking DAB cells (negative patches) are acquired from the same IHC tile after verifying segmentation detects no mitosis cells (Figure 3b). This balanced extraction strategy provides well-constructed patch pairs for training, with DAB-stained examples alongside negative patches. The two cell populations are now equally represented for GAN training.

3.4 | Generative Model for Virtual Restaining

We implemented a conditional generative adversarial network (cGAN) based on the Pix2Pix framework proposed by Isola et al. [38] for the task of translating H&E-stained slides to IHC-stained images. The generator follows a U-Net architecture with an encoder-decoder structure and addition of skip connections between mirrored layers in the encoder and decoder. This helps preserve low-level details in the output and allows reuse of spatial information from the input. The U-Net generator contains 8 downsampling layers with a base channel size of 64 and utilizes instance normalization. Dropout is also applied during training for added regularization. The discriminator employs a PatchGAN classifier [39] which views the image as a patchwork and predicts if each N×N patch is real or fake. This focuses the adversarial loss on local image structures rather than individual pixels. Our implementation uses a discriminator with three convolutional layers, an input channel size of 6 (concatenated H&E and IHC images), base channel size of 64 and instance normalization.

The model was trained with an adversarial LSGAN (Least Squares GAN) loss [40] combining the discriminator loss with a L1 pixel-wise loss between the generated and ground truth IHC images. This helps overcome limitations of L1 in producing blurry results while addressing artifacts from the adversarial loss alone. The loss weights are set at 100 for the L1 term. The network takes 256×256 RGB image patches as input, with a total of 102 776 patches split into training (75%) and validation (25%) set. To our knowledge, this represents the largest cohort of paired H&E and IHC images for virtual restaining to date.

Training was performed using the Adam solver with alternating gradient descent updates between the generator and discriminator. A batch size of 4 is used over 50 epochs, with validation every 100 iterations. Data augmentation including random flipping and rotation is also applied. After training, the best epoch was chosen as the one that provided the lowest root mean square error (RMSE) between synthetic and real patches on validation set.

The GAN model was then tested both on patches and larger tiles of size 1800×1800 pixels. To apply the generative model to tiles, we used the inference and center-cropping approach described in our previous work [41]. Briefly, a sliding window of 256 by 256 pixels was used, and only the central crop of 192×192 pixels was retained. The window was then slid over to the next patch with appropriate padding. Figure 4 illustrates the tile reconstruction process. The PyTorch framework (v1.13.1) was utilized for both training and testing purposes.

3.5 | Performance Metrics

Quantitative performance metrics were computed to assess the multi-stage registration framework and to evaluate the synthetic IHC images generated by the virtual restaining method. Images of different sizes were extracted to evaluate each step of the proposed method. Four types of evaluation metrics were used: (i) global IQA metrics, (ii) landmark-based TRE, (iii) novel local DAB intensity-based metrics, and (iv) clinical parameters such as mitotic count and quality score.

3.5.1 | Multi-Stage Registration Assessment

Several IQA metrics were computed between each registered H&E-PHH3 image pair. Structural similarity (SSIM) index and peak signal-to-noise ratio (PSNR) were used to assess image similarity [13]. Pearson's correlation coefficient (PCC) and mutual information (MI) were calculated to evaluate image correlation [16]. Intensity-based SSIM and PSNR are negatively influenced by different color appearance of H&E and IHC images, which is reflected on pixel intensity values. PCC and MI are better suited to evaluate the registration process. TRE is also used as evaluation metric to assess the accuracy of a paired-point registration. TRE is defined as the Euclidean distance between corresponding landmarks, manually annotated by an expert pathologist. A set of 25 points was manually reported for each H&E-PHH3 image pair at full resolution (40×) in the evaluation dataset.

In addition, we evaluated the following Y-biased weighted SSIM in YCbCr color space to focus on luminance values at the expense of chroma components:

$$wSSIM_{Y-bias} = 0.8 \cdot SSIM_Y + 0.1 \cdot SSIM_{Cb} + 0.1 \cdot SSIM_{Cr} \quad (1)$$

where $SSIM_Y$, $SSIM_{Cb}$, and $SSIM_{Cr}$ are SSIM values between H&E and PHH3 images for luminance, blue- and red-difference chroma components, respectively [42]. In the case of perfectly registered images, Y-biased weighted SSIM is equal to 1.0 since its definition is a linear convex combination of SSIM values.

3.5.2 | Virtual Restaining Assessment

Full-reference IQA metrics (PCC, SSIM, PSNR, and MI) were computed between real and synthetic PHH3 images to evaluate the virtual restaining process and for state-of-the-art direct performance comparison. Concerning the quantitative
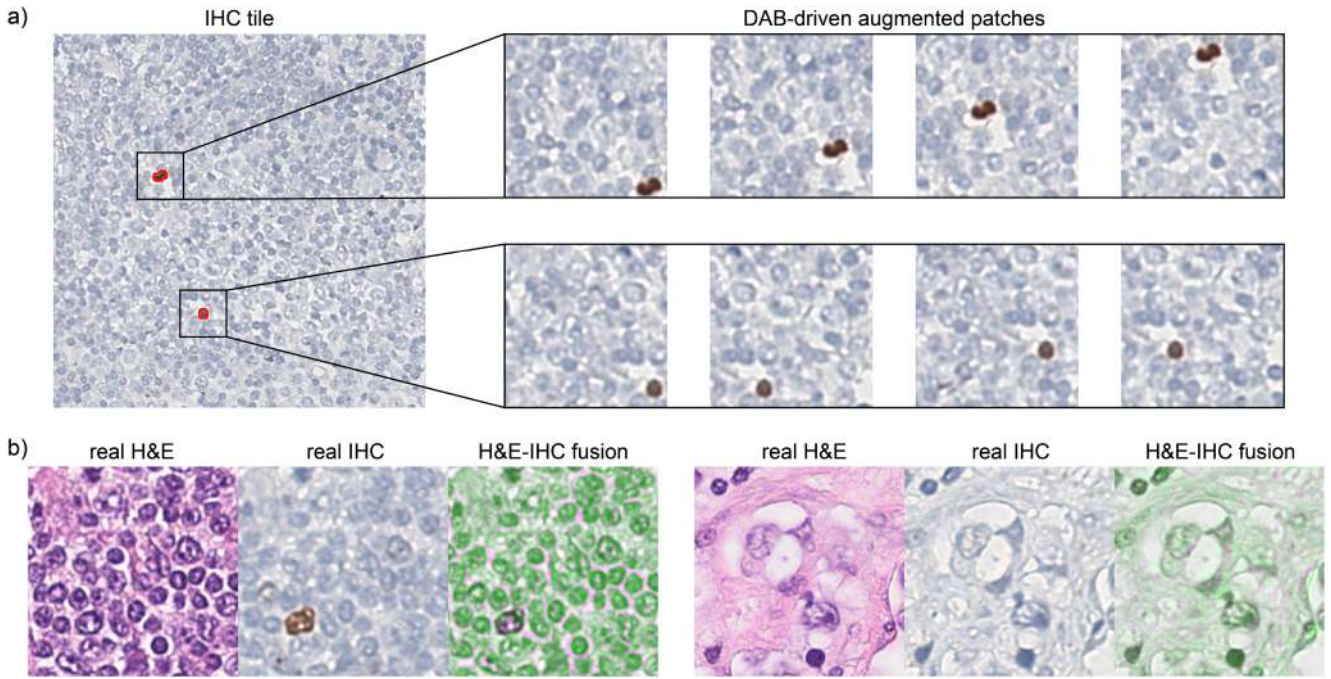
FIGURE 3 | Data preparation for the generative model. (a) DAB-driven patch extraction process. (b) Sample image pair of extracted patches with positive (left) and negative (right) IHC-staining.
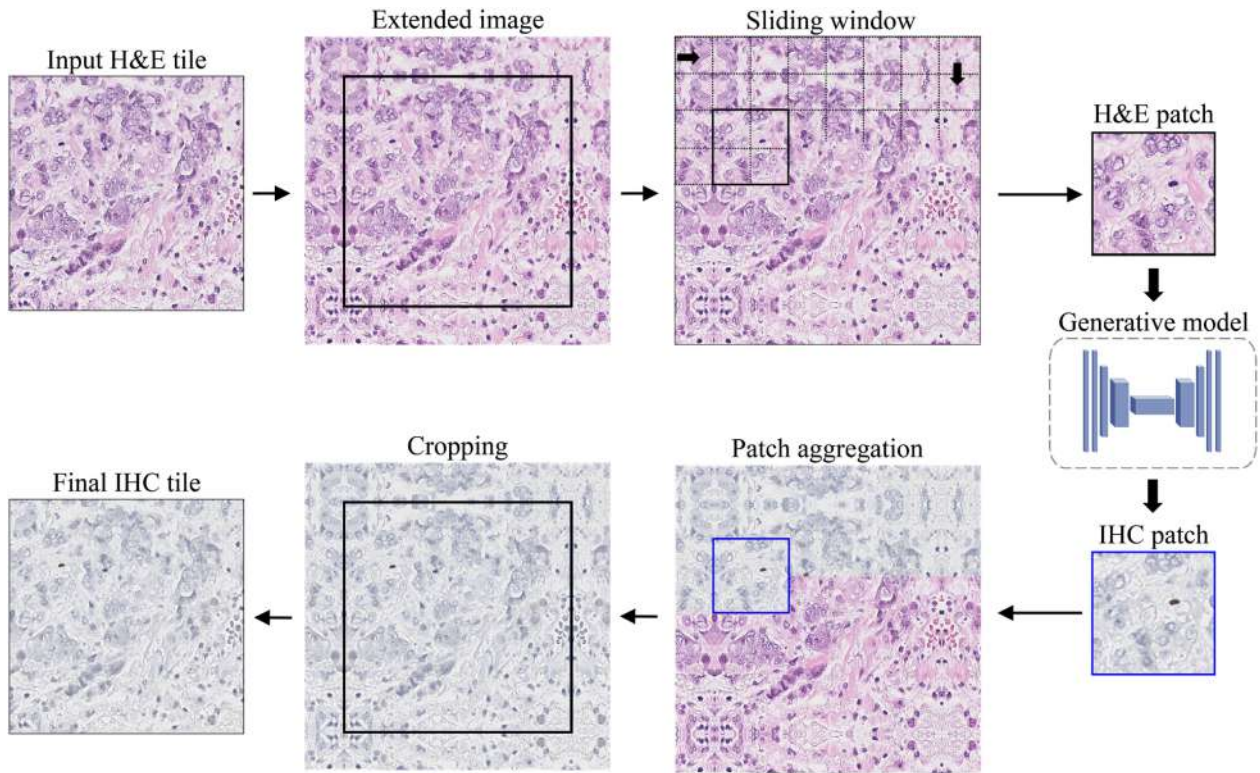

FIGURE 4 | Process for virtually restaining a tissue tile using the patch-trained GAN model. The input H&E tile is first extended by mirroring its boundaries. A sliding window inference is then performed, where the network generates IHC patches within a 256×256 window. For each window, only the central 192×192 region of the prediction is retained after cropping out boundary artifacts. Finally, cropping is applied to obtain the final IHC tile.

analysis, in addition to IQA metrics for similarity assessment, we propose a new local DAB intensity-based metric to focus on the chromogen (DAB) employed to stain PHH3

cells undergoing mitosis. A color deconvolution-based approach [43] is used to separate DAB channel from the hematoxylin counterstain. Since DAB intensity color spectrum is

most strongly represented in the red chroma component, we computed the following Cr-biased weighted SSIM in YCbCr color space:

$$wSSIM_{Cr-bias} = 0.1 \cdot SSIM_Y + 0.1 \cdot SSIM_{Cb} + 0.8 \cdot SSIM_{Cr} \quad (2)$$

where SSIM values were computed between DAB channels of original and synthetic PHH3 images, obtained using color deconvolution technique. In the case of perfectly registered images, Cr-biased weighted SSIM is equal to 1.0 since its definition is a linear convex combination of SSIM values. In addition, another DAB intensity-based metric was proposed for the quantitative analysis. Color distance (CDIST) is defined as the Euclidean distance between the average color of each DAB-stained cell in the real IHC image and the corresponding synthetic one. DAB-stained cells were annotated by an expert pathologist for all test images. Higher values of CDIST denote a worse DAB intensity color correspondence between real and synthetic mitotic instances.

From a clinical perspective, by evaluation of an expert pathologist, mitotic count, and image quality were also assessed for real and synthetic IHC images. The mitotic count is defined as the number of DAB-stained cells undergoing mitosis, while image quality was graded with a score of "1: bad," "2: poor," "3: acceptable," "4: good," and "5: excellent."

4 | Results

Table 1 summarizes the composition of the evaluation image dataset. All images are extracted at full magnification (40×) to best assess cellular structures. The evaluation metrics computed to assess each task are described in the following subsections. As shown in Table 1, the image field of view (FoV) is progressively reduced to focus on cellular structures at the end of the pipeline.

4.1 | Quantitative Results for Multi-Stage Registration

Each step of the multi-stage registration framework was assessed by computing IQA evaluation metrics. All metrics were computed by extracting images of different FoVs at full magnification (40×). The 1st stage task evaluated both macro- and micro-registration using 108 images of size 4000×4000 pixels. The 2nd stage was assessed on 1462 images of size 2000×2000 pixels. Image field registration took approximately 57 s per H&E-PHH3 pair of size 2000×2000 pixels. Figure 5 shows a visual analysis of the multi-stage registration process.

Table 2 reports the quantitative metrics for each registration task. Higher metric values denote better registration alignment, except for TRE for which lower values are considered better. The micro-registration step improved PCC value of 23.5% and a further increase of 11.8% was observed after the final 2nd stage registration step. SSIM and PSNR also increased with each subsequent registration step, though the gains were smaller than for PCC. MI scores had the largest improvement between 1st and 2nd registration, nearly doubling from 0.618 to 0.918. MI is especially sensitive to non-linear mappings, suggesting the final step best captured complex tissue deformations. TRE, reported in physical units, shows a decrease of 75% between macro and micro-registration and a further decrease of 58% in the last registration stage. wSSIM$_{Y-bias}$ shows a better increase in absolute terms with respect to standard SSIM since more weight is given in the computation of luminance component, thus it is less affected by different color appearance of H&E and PHH3 images. Each step of the proposed multi-registration framework is useful for achieving final pixel-level cellular matching.

4.2 | Quantitative Results for Virtual Restaining

The performance of the proposed virtual restaining method was evaluated using both global IQA metrics and novel local DAB intensity-based metrics. From the test set, we generated and evaluated a total of 130 virtual restained images of size 1800×1800 pixels. Table 3 presents the quantitative results achieved by our method on the test set, compared with state-of-the-art AI methods.

On average, the mean IQA metric scores were high, indicating very good alignment between real and virtually restained images. Additionally, low standard deviations across metrics suggest consistent performance between images. Regarding DAB-based metrics, wSSIM$_{Cr-bias}$ nearing 1.0 demonstrates the GAN accurately reproduced DAB color mappings globally. However, the larger standard deviation for CDIST implies greater variability in local DAB intensity distributions between images.

Compared to other state-of-the-art AI methods, our proposed model outperforms them across all quantitative metrics, demonstrating its superior performance in generating high-quality virtual PHH3 staining. The Style transfer network [4] achieves the lowest scores among the compared methods, with an SSIM of 0.678 and a PSNR of 25.51 dB. The Pyramid GAN [29] and Conditional GAN [28] show improved performance, with SSIM values of 0.724 and 0.739, and PSNR values of 26.54 and 26.47 dB, respectively. However, our proposed

TABLE 1 | Evaluation image dataset composition.

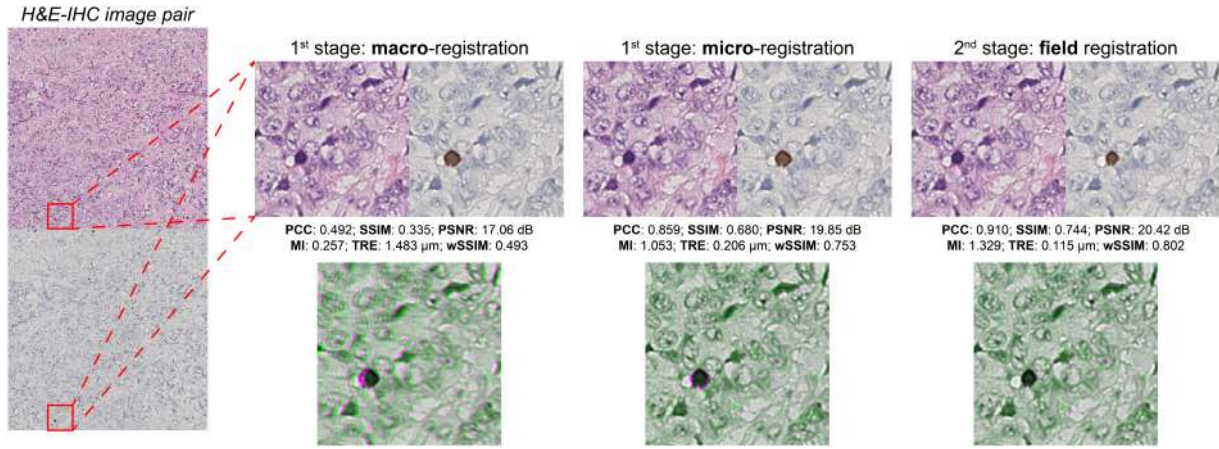| Task	Tissue	# Images	Image size (pixels)	Evaluation metrics
1st stage: macro-registration	Lymph nodes, Bladder	108	4000×4000	IQA, TRE wSSIM in YCbCr
1st stage: micro-registration				
2nd stage: field registration		1462	2000×2000	
Virtual restaining	Bladder	130	1800×1800	IQA, DAB intensity-based Mitotic count, Quality score

FIGURE 5 | Results for each step of the multi-stage registration framework (i.e., macro-, micro-, and field registration). Zoomed-in views of the H&E-PHH3 image pair are shown at top, and the resulting image fusion from aligning the pair is shown at bottom, with associated quantitative metrics.

TABLE 2 | Validation of the multi-stage registration framework. Average quantitative metrics (± standard deviation) are reported.

Task	IQA metrics				Landmark	YCbCr
	PCC	SSIM	PSNR (dB)	MI	TRE (µm)	wSSIM
1st stage: macro at 1.25×	0.467 (±0.155)	0.322 (±0.108)	17.18 (±2.065)	0.290 (±0.183)	1.177 (±0.668)	0.461 (±0.093)
1st stage: micro at 2.5×	0.702 (±0.093)	0.500 (±0.086)	18.50 (±2.026)	0.618 (±0.211)	0.289 (±0.100)	0.601 (±0.072)
2nd stage at 40×	0.820 (±0.058)	0.612 (±0.082)	19.13 (±2.593)	0.918 (±0.212)	0.122 (±0.022)	0.679 (±0.070)

TABLE 3 | Comparison of the proposed model with other state-of-the-art AI methods for virtual restaining. Average quantitative metrics (± standard deviation) are provided for the assessment of virtual restaining quality. The best performances are highlighted in bold.

Method	IQA metrics				DAB-based	
	PCC	SSIM	PSNR (dB)	MI	wSSIM	CDIST
Style transfer network [4]	0.794 (±0.054)	0.678 (±0.032)	25.51 (±0.560)	0.762 (±0.167)	0.947 (±0.006)	46.00 (±42.17)
Pyramid GAN [29]	0.840 (±0.036)	0.724 (±0.030)	26.54 (±0.565)	0.894 (±0.142)	0.948 (±0.007)	49.40 (±41.67)
Conditional GAN [28]	0.844 (±0.043)	0.739 (±0.035)	26.47 (±0.579)	0.949 (±0.173)	0.945 (±0.008)	47.44 (±40.60)
Proposed model	**0.913** (±0.023)	**0.861** (±0.018)	**29.70** (±0.815)	**1.339** (±0.180)	**0.974** (±0.008)	**44.53** (±41.24)

model surpasses all these methods, achieving an SSIM of 0.861 and a PSNR of 29.70 dB, indicating a higher level of structural similarity and signal quality in the virtually restained images. Furthermore, our model achieves the highest PCC and MI scores, suggesting a strong correlation and information sharing between the virtual and real staining. The wSSIM score of 0.974 further confirms the accurate reproduction of DAB color mappings in our model. The lowest CDIST value of 44.53 for our model, compared with the other methods, demonstrates a better match in local DAB intensity distributions between the virtual and real staining.

Figure 6a,b shows sample results from evaluating the virtual restaining approach. It presents real H&E and paired PHH3-IHC images alongside the corresponding synthetically generated images. Global and local quantitative metrics are also shown for visual assessment purposes. Figure 6c presents the histogram distribution of CDIST values calculated over DAB-stained cells.

We further analyzed the color distribution of the virtually PHH3-stained images by converting them from RGB to YCbCr color space [21]. Figure 7 shows the histogram distributions of the Cb
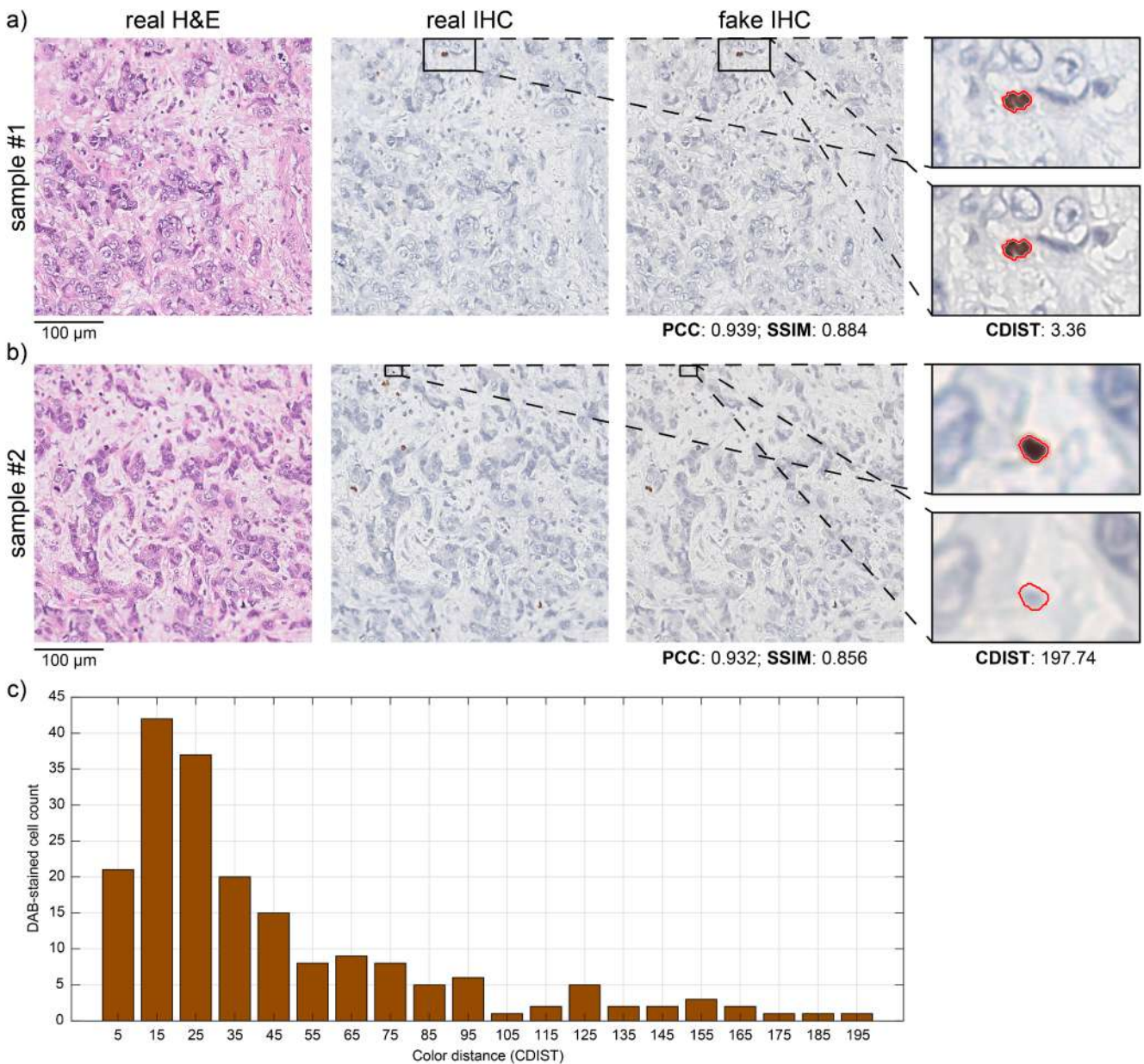
FIGURE 6 | Sample images showcasing quantitative metrics for virtual restaining assessment: Presenting both the best case—sample#1 (a)—and a faulty case—sample#2 (b)—of functional transfer. Additionally, zoomed-in views are provided for a direct comparison of real and synthetic PHH3-stained mitotic cells, contoured in red. (c) Histogram distribution of color distance metric for all DAB-stained cells.

and Cr chroma channels, which represent the blue and red information, respectively. Examining the Cb and Cr chroma channels confirmed that the GAN successfully reproduced the characteristic color distributions seen in real H&E and IHC samples.

4.3 | Assessment of Mitotic Count and Image Quality Score

An expert pathologist also qualitatively assessed the clinical accuracy of virtual restaining for tissue analysis tasks. The pathologist compared the mitotic count in synthetic images to the corresponding real PHH3-IHC images. Additionally, image quality was evaluated qualitatively on a 5-point qualitative scale ("1: bad," "2: poor," "3: acceptable," "4: good," and "5: excellent").

Figure 8 reports the mitotic count and quality scores between real and synthetic images. The PCC for mitotic counts was 0.792. On average, synthetic and real images received scores of 4.45 and 3.71, respectively. In 98% of cases, the pathologist rated synthetic image quality as equal or higher than the real image quality. This side-by-side evaluation by an expert validated that the synthetic images accurately represented mitotic activity and achieved perceptual quality equivalent or better than real staining for clinical use.

5 | Discussion

This study aimed to develop and evaluate a novel experimental automated method for functional virtual restaining of digital
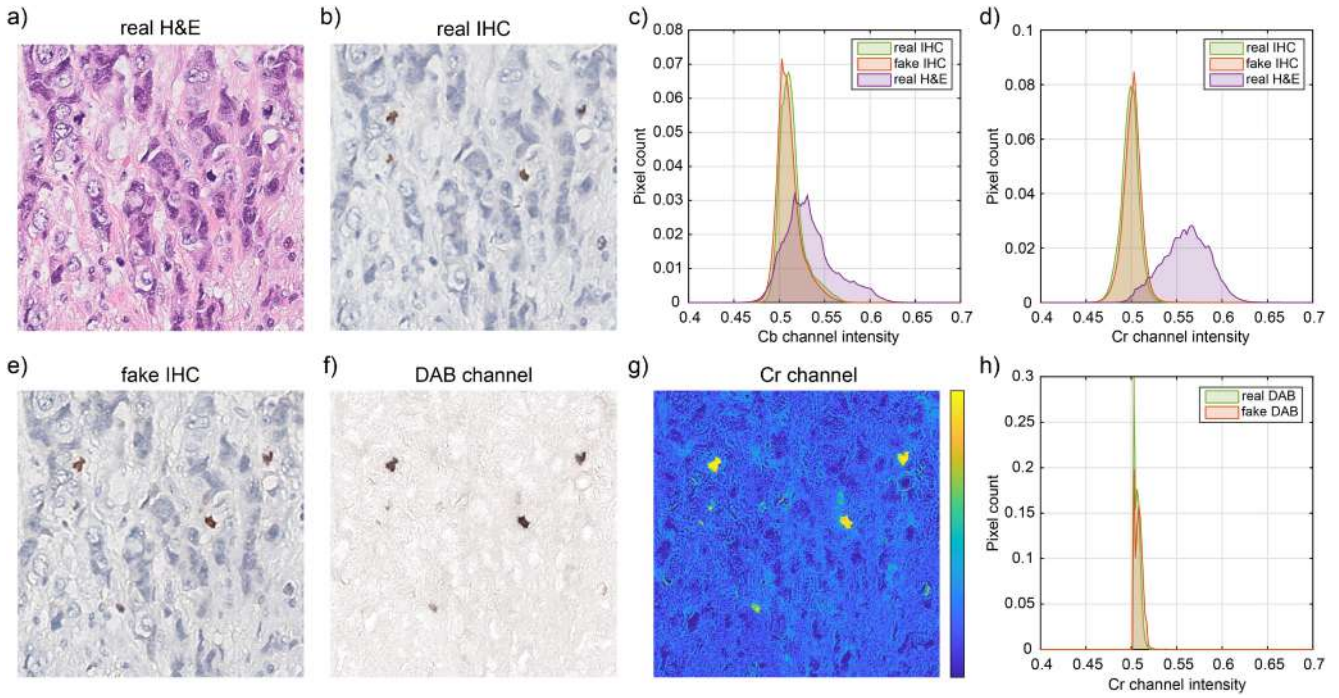
FIGURE 7 | Histogram analysis in YCbCr color space. (a, b) Real H&E and IHC images; (c, d) Cb and Cr channel histogram distributions for real and synthetic images. (e) Synthetic PHH3-stained image generated by the GAN model; (f) DAB staining intensities extracted via color deconvolution; (g, h) Cr channel of synthetic image and Cr histogram comparison of real and synthetic DAB intensity images.
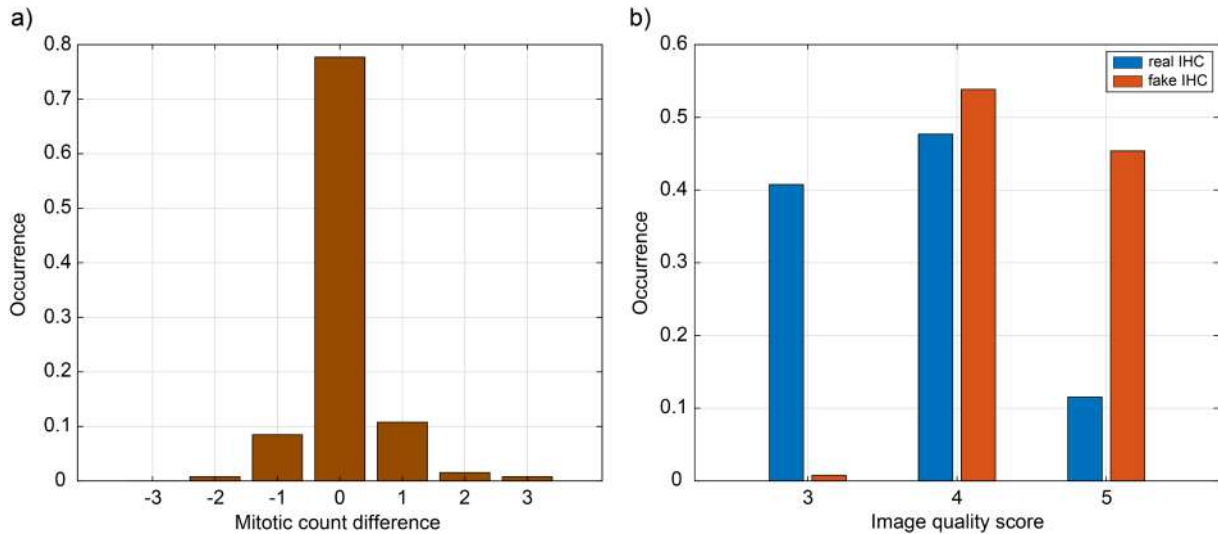

FIGURE 8 | Clinical analysis presenting the difference in mitotic count between synthetic and real PHH3-stained images (a), along with corresponding image quality scores (b).

pathology slides. Our model is based on a multi-stage registration framework that aligns histological slices and a generative model that creates realistic synthetic images of the target stain. To the best of our knowledge, this is the first study to propose a deep learning-based generative model with extensive validation both from a quantitative perspective and clinical implications.

The multi-stage registration framework leveraged coarse and fine-scale alignment techniques at varying magnifications to gradually improve matching between structures. PCC improved from 0.467 at 1.25× to 0.702 at 2.5×, validating the benefit of

higher magnification refinement (Table 2). Field registration at 40× provided a further boost to 0.820, demonstrating the cumulative gains from stepwise alignment. MI also increased after completion of the two registration stages, showing improved ability to capture non-linear tissue deformations. Thanks to this two-step approach we were able to achieve pixel-level correspondence between cellular structures while avoiding computational limitations.

The GAN model learned to translate H&E slides to realistic synthetic PHH3 images, as shown through strong quantitative and

qualitative alignment scores. Global IQA metrics exceeded 0.91 for PCC, 0.86 for SSIM and 29.7 dB for PSNR, validating good overall similarity (Table 3). It is important to note that the global image quality metrics reported in this study aim to quantify the similarity between the virtual and real staining in terms of overall image attributes such as color distribution, sharpness, and contrast. The higher scores for the virtual staining indicate that our generative model successfully captures and reproduces these general image properties from the real PHH3 staining. However, these metrics do not directly assess the functional quality or accuracy of the virtual staining itself. For the purpose of evaluating the functional quality of the virtual staining, we introduced novel stain-specific metrics to assess the precision and sensitivity of mitotic figure labeling in the virtual PHH3 images. These metrics further confirmed accurate reproduction of global and localized DAB patterns (average $wSSIM_{Cr-bias}$ of 0.974 ± 0.008), though some synthetic cells differed more from real counterparts, indicating room for improvement in consistency (Figure 6). Our model quantitatively outperforms other state-of-the-art AI methods proposed for virtual restaining.

Pathologist scores confirmed synthetic images provided high quality representations suitable for diagnostic tasks, with mitotic counts well-correlated overall and quality approaching real IHC images (Figure 8). However, a small overestimation risk was noted, warranting optimization to distinguish atypical nuclei. Specifically, some non-tumor cells with very dense chromatin, such as neutrophils, or multilobed nuclei similar to atypical neoplastic mitoses, are transformed into tumor mitoses by the generative model. Further refinements to the model architecture and training process could help distinguish these challenging nuclei. Nevertheless, this phenomenon is extremely limited, with no more than an additional count compared to the real ones.

Our study makes several key contributions. First, we employed a multi-stage registration approach to achieve precise pixel-wise matching between cellular and subcellular structures from the source H&E and target IHC stains. Accurate image alignment is critical, as it ensures corresponding structures are properly mapped during virtual restaining. Second, we trained a deep learning-based generative model on paired data, enabling the transfer of functional information at the single cell level. Unlike previous methods that focused solely on stain style-transfer, our model considers both morphological and functional attributes of individual cells by learning from cell-to-cell mappings from the paired training data.

The proposed virtual restaining method has significant clinical implications in the field of digital pathology. One key clinical application is the assessment of mitotic activity, which is crucial for tumor grading and prognosis. Our method allows for the virtual generation of PHH3 staining, specifically highlighting cells undergoing mitosis. The strong correlation observed between mitotic counts derived from synthetic and physical PHH3 staining validates the reliability of our approach for this critical task. Furthermore, the ability to generate multiple virtual stains from a single H&E slide can enhance the efficiency and cost-effectiveness of pathology laboratories. Instead of performing multiple physical staining procedures, pathologists can leverage our virtual restaining method to obtain comprehensive morphological and functional information from a single digital slide.

This can lead to reduced turnaround times and optimized resource utilization.

The proposed pipeline is also scalable and can be easily extended to additional IHC biomarkers such as p53 or other histochemical stains like PAS or trichrome. In terms of computational efficiency, the method takes only approximately 1.27 s to process the staining of an 1800 × 1800 tile.

However, some limitations of the current approach should be acknowledged. In this study, we focused on generating synthetic PHH3 images from H&E-stained sections of human lymph nodes and bladder tissue only. While these tissue types demonstrate the approach's potential, future studies must validate it across more tissue types and disease states. Moreover, the registration step required to build the paired training dataset is computationally intensive. However, once trained, the generative model directly translates an H&E image into the corresponding synthetic IHC image without need for further registration or alignment. Finally, although using destained-restained sections enables precise alignment, consecutive sections may be more readily available in clinical practice. Future research will expand the handled pairs to consecutive sections of primary organs like the liver and kidney.

Currently, our research group is actively working on expanding this approach to enable the processing of entire whole-slide images. With our proposed algorithm, starting from a single H&E section, we aim to generate all the special stainings associated with that tissue, while also preserving the functional information conveyed by these stains. This extension will provide a comprehensive and efficient solution for virtual restaining of large-scale digital pathology images, enabling pathologists to obtain a wealth of valuable information from a single H&E slide.

6 | Conclusion

In conclusion, we have presented a novel approach for virtual enhanced digital pathology through functional restaining. Our multi-stage registration framework, combined with a deep learning-based generative model, allows for the transfer of functional information between stains, enabling a comprehensive assessment of cellular structures from both morphological and functional perspectives. The extensive quantitative and clinical validation of our method demonstrates its accuracy and potential for diagnostic applications. While still limited in scope, this research presents an important initial step toward automated multiparameter analysis of digitized histology with applications in efficiency, sample preservation, and simultaneous biomarker examination. Future research directions include exploring the application of our approach to different staining modalities and further investigating its impact on various pathological assessments.

Author Contributions

Conceptualization: Massimo Salvi, Filippo Molinari. Data curation: Nicola Michielli, Alessandro Mogetta. Formal analysis: Massimo Salvi, Nicola Michielli, Lorenzo Salamone. Methodology: Massimo

Salvi, Nicola Michielli. Resources: Alessandro Gambella, Luca Molinaro, Mauro Papotti. Software: Massimo Salvi, Lorenzo Salamone. Supervision: Massimo Salvi, Filippo Molinari. Validation: Nicola Michielli, Lorenzo Salamone, Alessandro Gambella. Visualization: Massimo Salvi, Nicola Michielli. Writing – original draft: Massimo Salvi, Nicola Michielli. Writing – review and editing: Lorenzo Salamone, Alessandro Mogetta, Alessandro Gambella, Mauro Papotti, Filippo Molinari.

Conflicts of Interest

Massimo Salvi and Filippo Molinari disclose a relationship with AEQUIP srl, which includes equity. Nicola Michielli reports a relationship with AEQUIP srl, which includes nonfinancial support. Alessandro Mogetta reports a relationship with AEQUIP srl, which includes employment. The remaining authors declare no known competing financial interests or personal relationships that could have appeared to influence the work reported in this paper.

Data Availability Statement

The data that support the findings of this study are available from the corresponding author upon reasonable request.

References

1. I. Clark and M. S. Torbenson, "Immunohistochemistry and Special Stains in Medical Liver Pathology," *Advances in Anatomic Pathology* 24, no. 2 (2017): 99–109, https://doi.org/10.1097/PAP.0000000000000139.

2. J. A. Ramos-Vara and M. A. Miller, "When Tissue Antigens and Antibodies Get Along: Revisiting the Technical Aspects of Immunohistochemistry—The Red, Brown, and Blue Technique," *Veterinary Pathology* 51, no. 1 (2014): 42–87, https://doi.org/10.1177/0300985813505879.

3. G. A. Giannico and O. Hameed, "Evaluation of Prostate Needle Biopsies," in *Molecular & Diagnostic Imaging in Prostate Cancer. Advances in Experimental Medicine and Biology*, 126, ed. H. Schatten (Cham: Springer, 2018), 69–86, https://doi.org/10.1007/978-3-319-99286-0_4.

4. K. de Haan, Y. Zhang, J. E. Zuckerman, et al., "Deep Learning-Based Transformation of H&E Stained Tissues Into Special Stains," *Nature Communications* 12, no. 1 (2021): 4884, https://doi.org/10.1038/s41467-021-25221-2.

5. T. Mathew, B. Ajith, J. R. Kini, and J. Rajan, "Deep Learning-Based Automated Mitosis Detection in Histopathology Images for Breast Cancer Grading," *International Journal of Imaging Systems and Technology* 32, no. 4 (2022): 1192–1208, https://doi.org/10.1002/ima.22703.

6. E. Duregon, L. Molinaro, M. Volante, et al., "Comparative Diagnostic and Prognostic Performances of the Hematoxylin-Eosin and Phospho-Histone H3 Mitotic Count and Ki-67 Index in Adrenocortical Carcinoma," *Modern Pathology* 27, no. 9 (2014): 1246–1254, https://doi.org/10.1038/modpathol.2013.230.

7. D. J. Meuten, F. M. Moore, and J. W. George, "Mitotic Count and the Field of View Area: Time to Standardize," *Veterinary Pathology* 53, no. 1 (2016): 7–9, https://doi.org/10.1177/0300985815593349.

8. N. Tancredi-Cueto, G. Vigil-Bastitta, R. Bologna-Molina, and V. Beovide-Cortegoso, "The Value of Phosphohistone H3 as a Cell Proliferation Marker in Oral Squamous Cell Carcinoma. A Comparative Study With Ki-67 and the Mitotic Activity Index," *Medicina Oral, Patología Oral y Cirugía Bucal* 27, no. 5 (2022): e444–e451, https://doi.org/10.4317/medoral.25420.

9. O. Ardon, M. Labasin, M. Friedlander, et al., "Quality Management System in Clinical Digital Pathology Operations at a Tertiary Cancer Center," *Laboratory Investigation* 103, no. 11 (2023): 100246, https://doi.org/10.1016/j.labinv.2023.100246.

10. M. Cui and D. Y. Zhang, "Artificial Intelligence and Computational Pathology," *Laboratory Investigation* 101, no. 4 (2021): 412–422, https://doi.org/10.1038/s41374-020-00514-0.

11. A. Shmatko, N. Ghaffari Laleh, M. Gerstung, and J. N. Kather, "Artificial Intelligence in Histopathology: Enhancing Cancer Research and Clinical Oncology," *Nature Cancer* 3, no. 9 (2022): 1026–1038, https://doi.org/10.1038/s43018-022-00436-4.

12. L. Latonen, S. Koivukoski, U. Khan, and P. Ruusuvuori, "Virtual Staining for Histology by Deep Learning," in *Trends in Biotechnology* (Amsterdam, Netherlands: Elsevier, 2024), https://doi.org/10.1016/j.tibtech.2024.02.009.

13. B. Bai, X. Yang, Y. Li, Y. Zhang, N. Pillar, and A. Ozcan, "Deep Learning-Enabled Virtual Histological Staining of Biological Samples," *Light: Science & Applications* 12, no. 1 (2023): 57, https://doi.org/10.1038/s41377-023-01104-7.

14. Z. Xu, X. Huang, C. F. Moro, B. Bozóky, and Q. Zhang, "GAN-Based Virtual Re-Staining: A Promising Solution for Whole Slide Image Analysis," *ArXiv* (2019), https://doi.org/10.48550/arXiv.1901.04059.

15. C. R. Jackson, A. Sriharan, and L. J. Vaickus, "A Machine Learning Algorithm for Simulating Immunohistochemistry: Development of SOX10 Virtual IHC and Evaluation on Primarily Melanocytic Neoplasms," *Modern Pathology* 33, no. 9 (2020): 1638–1648, https://doi.org/10.1038/s41379-020-0526-z.

16. A. Su, A. Lee, X. Tan, et al., "A Deep Learning Model for Molecular Label Transfer That Enables Cancer Cell Identification From Histopathology Images," *npj Precision Oncology* 6, no. 1 (2022): 14, https://doi.org/10.1038/s41698-022-00252-0.

17. C.-W. Wang, Y.-C. Lee, M.-A. Khalil, K.-Y. Lin, C.-P. Yu, and H.-C. Lien, "Fast Cross-Staining Alignment of Gigapixel Whole Slide Images With Application to Prostate Cancer and Breast Cancer Analysis," *Scientific Reports* 12, no. 1 (2022): 11623, https://doi.org/10.1038/s41598-022-15962-5.

18. Y. Rivenson, H. Wang, Z. Wei, et al., "Virtual Histological Staining of Unlabelled Tissue-Autofluorescence Images Via Deep Learning," *Nature Biomedical Engineering* 3, no. 6 (2019): 466–477, https://doi.org/10.1038/s41551-019-0362-y.

19. D. Li, H. Hui, Y. Zhang, et al., "Deep Learning for Virtual Histological Staining of Bright-Field Microscopic Images of Unlabeled Carotid Artery Tissue," *Molecular Imaging and Biology* 22, no. 5 (2020): 1301–1309, https://doi.org/10.1007/s11307-020-01508-6.

20. N. Pillar and A. Ozcan, "Virtual Tissue Staining in Pathology Using Machine Learning," *Expert Review of Molecular Diagnostics* 22, no. 11 (2022): 987–989, https://doi.org/10.1080/14737159.2022.2153040.

21. Y. Zhang, L. Huang, T. Liu, et al., "Virtual Staining of Defocused Autofluorescence Images of Unlabeled Tissue Using Deep Neural Networks," *Intelligent Computing* 2022 (2024): 1–13, https://doi.org/10.34133/2022/9818965.

22. B. Bai, H. Wang, Y. Li, et al., "Label-Free Virtual HER2 Immunohistochemical Staining of Breast Tissue Using Deep Learning," *BME Frontiers* 2022 (2022): 9786242, https://doi.org/10.34133/2022/9786242.

23. J. Salido, N. Vallez, L. González-López, O. Deniz, and G. Bueno, "Comparison of Deep Learning Models for Digital H&E Staining From Unpaired Label-Free Multispectral Microscopy Images," *Computer Methods and Programs in Biomedicine* 235 (2023): 107528, https://doi.org/10.1016/j.cmpb.2023.107528.

24. A. Rana, A. Lowe, M. Lithgow, et al., "Use of Deep Learning to Develop and Analyze Computational Hematoxylin and Eosin Staining of Prostate Core Biopsy Images for Tumor Diagnosis," *JAMA Network Open* 3, no. 5 (2020): e205111, https://doi.org/10.1001/jamanetworkopen.2020.5111.

25. Y. Li, N. Pillar, J. Li, et al., "Virtual Histological Staining of Unlabeled Autopsy Tissue," *Nature Communications* 15, no. 1 (2024): 1684, https://doi.org/10.1038/s41467-024-46077-2.

26. N. Pillar, Y. Li, Y. Zhang, and A. Ozcan, "Virtual Staining of Nonfixed Tissue Histology," *Modern Pathology* 37, no. 5 (2024): 100444, https://doi.org/10.1016/j.modpat.2024.100444.

27. S. Liu, B. Zhang, Y. Liu, et al., "Unpaired Stain Transfer Using Pathology-Consistent Constrained Generative Adversarial Networks," *IEEE Transactions on Medical Imaging* 40, no. 8 (2021): 1977–1989, https://doi.org/10.1109/TMI.2021.3069874.

28. C. Mercan, G. C. A. M. Mooij, D. Tellez, et al., "Virtual Staining for Mitosis Detection in Breast Histopathology," in *2020 IEEE 17th International Symposium on Biomedical Imaging (ISBI)* (Iowa City, USA: IEEE, 2020), 1770–1774, https://doi.org/10.1109/ISBI45749.2020.9098409.

29. S. Liu, C. Zhu, F. Xu, X. Jia, Z. Shi, and M. Jin, "BCI: Breast Cancer Immunohistochemical Image Generation Through Pyramid Pix2pix," in *2022 IEEE/CVF Conference on Computer Vision and Pattern Recognition Workshops (CVPRW)* (New Orleans, USA: IEEE, 2022), https://doi.org/10.1109/CVPRW56347.2022.00198.

30. J. Vasiljević, Z. Nisar, F. Feuerhake, C. Wemmert, and T. Lampert, "CycleGAN for Virtual Stain Transfer: Is Seeing Really Believing?," *Artificial Intelligence in Medicine* 133 (2022): 102420, https://doi.org/10.1016/j.artmed.2022.102420.

31. R. Yan, Q. He, Y. Liu, et al., "Unpaired Virtual Histological Staining Using Prior-Guided Generative Adversarial Networks," *Computerized Medical Imaging and Graphics* 105 (2023): 102185, https://doi.org/10.1016/j.compmedimag.2023.102185.

32. R. Zhang, Y. Cao, Y. Li, et al., "MVFStain: Multiple Virtual Functional Stain Histopathology Images Generation Based on Specific Domain Mapping," *Medical Image Analysis* 80 (2022): 102520, https://doi.org/10.1016/j.media.2022.102520.

33. M. Gadermayr, L. Gupta, V. Appel, P. Boor, B. M. Klinkhammer, and D. Merhof, "Generative Adversarial Networks for Facilitating Stain-Independent Supervised and Unsupervised Segmentation: A Study on Kidney Histology," *IEEE Transactions on Medical Imaging* 38, no. 10 (2019): 2293–2302, https://doi.org/10.1109/TMI.2019.2899364.

34. C. D. Gatenbee, A.-M. Baker, S. Prabhakaran, et al., "VALIS: Virtual Alignment of PathoLogy Image Series," *BioRxiv* (2021), https://doi.org/10.1101/2021.11.09.467917.

35. C. D. Gatenbee, A.-M. Baker, S. Prabhakaran, et al., "Virtual Alignment of Pathology Image Series for Multi-Gigapixel Whole Slide Images," *Nature Communications* 14, no. 1 (2023): 4502, https://doi.org/10.1038/s41467-023-40218-9.

36. C. Li, Z. Li, Z. Wang, et al., "Comprehensive Color Solutions: CAM16, CAT16, and CAM16-UCS," *Color Research & Application* 42, no. 6 (2017): 703–718, https://doi.org/10.1002/col.22131.

37. M. Salvi, N. Michielli, K. M. Meiburger, et al., "Cyto-Knet: An Instance Segmentation Approach for Multiple Myeloma Plasma Cells Using Conditional Kernels," *International Journal of Imaging Systems and Technology* 34, no. 1 (2024): e22984, https://doi.org/10.1002/ima.22984.

38. P. Isola, J.-Y. Zhu, T. Zhou, and A. A. Efros, "Image-to-Image Translation With Conditional Adversarial Networks," in *2017 IEEE Conference on Computer Vision and Pattern Recognition (CVPR)* (Honolulu, USA: IEEE, 2017), 5967–5976, https://doi.org/10.1109/CVPR.2017.632.

39. C. Li and M. Wand, "Precomputed Real-Time Texture Synthesis With Markovian Generative Adversarial Networks BT—Computer Vision—ECCV 2016" (2016).

40. X. Mao, Q. Li, H. Xie, R. Y. K. Lau, Z. Wang, and S. P. Smolley, "Least Squares Generative Adversarial Networks," in *2017 IEEE International Conference on Computer Vision (ICCV)* (Venice, Italy: IEEE, 2017), https://doi.org/10.1109/ICCV.2017.304.

41. M. Salvi, A. Mogetta, A. Gambella, et al., "Automated Assessment of Glomerulosclerosis and Tubular Atrophy Using Deep Learning," *Computerized Medical Imaging and Graphics* 90 (2021): 101930, https://doi.org/10.1016/j.compmedimag.2021.101930.

42. S. Biswas and S. Barma, "Feature Fusion GAN Based Virtual Staining on Plant Microscopy Images," *IEEE/ACM Transactions on Computational Biology and Bioinformatics* (2024): 1–11, https://doi.org/10.1109/TCBB.2024.3380634.

43. M. Salvi, N. Michielli, and F. Molinari, "Stain Color Adaptive Normalization (SCAN) Algorithm: Separation and Standardization of Histological Stains in Digital Pathology," *Computer Methods and Programs in Biomedicine* 193 (2020): 105506, https://doi.org/10.1016/j.cmpb.2020.105506.